On the loss mechanisms of radiation belt electron dropouts during the 12 September 2014 geomagnetic storm

Xin Ma[1], Zheng Xiang[1*], BinBin Ni[1,2*], Song Fu[1], Xing Cao[1], Man Hua[1], DeYu Guo[1], YingJie Guo[1], XuDong Gu[1], ZeYuan Liu[1], and Qi Zhu[1]

[1]Department of Space Physics, School of Electronic Information, Wuhan University, Wuhan 430072, China;

[2]Chinese Academy of Sciences Center for Excellence in Comparative Planetology, Hefei 230026, China

Key Points:
- The loss mechanisms of radiation belt dropout during the 12 September 2014 storm were investigated using satellite measurements
- During the initial phase of the storm, magnetopause shadowing was the dominant loss mechanism, supported by energy-independent decay and butterfly pitch angle distributions (PADs)
- The wave–particle interactions played an important role in >1 MeV electron loss during the main phase of the storm and produced 90-peaked PADs at $L < 4$

Abstract: Radiation belt electron dropouts indicate electron flux decay to the background level during geomagnetic storms, which is commonly attributed to the effects of wave-induced pitch angle scattering and magnetopause shadowing. To investigate the loss mechanisms of radiation belt electron dropouts triggered by a solar wind dynamic pressure pulse event on 12 September 2014, we comprehensively analyzed the particle and wave measurements from Van Allen Probes. The dropout event was divided into three periods: before the storm, the initial phase of the storm, and the main phase of the storm. The electron pitch angle distributions (PADs) and electron flux dropouts during the initial and main phases of this storm were investigated, and the evolution of the radial profile of electron phase space density (PSD) and the (μ, K) dependence of electron PSD dropouts (where μ, K, and L^* are the three adiabatic invariants) were analyzed. The energy-independent decay of electrons at $L > 4.5$ was accompanied by butterfly PADs, suggesting that the magnetopause shadowing process may be the major loss mechanism during the initial phase of the storm at $L > 4.5$. The features of electron dropouts and 90°-peaked PADs were observed only for >1 MeV electrons at $L < 4$, indicating that the wave-induced scattering effect may dominate the electron loss processes at the lower L-shell during the main phase of the storm. Evaluations of the (μ, K) dependence of electron PSD drops and calculations of the minimum electron resonant energies of H+-band electromagnetic ion cyclotron (EMIC) waves support the scenario that the observed PSD drop peaks around $L^* = 3.9$ may be caused mainly by the scattering of EMIC waves, whereas the drop peaks around $L^* = 4.6$ may result from a combination of EMIC wave scattering and outward radial diffusion.

Keywords: radiation belt electron flux dropouts; geomagnetic storm; electron phase space density; magnetopause shadowing; wave–particle interactions

1. Introduction

Earth's outer radiation belt is full of energetic electrons, from hundreds of kiloelectron volts (keV) to several megaelectron volts (MeV). These high-energy electrons pose a potential hazard to spacecraft operations and astronauts. The radiation belt electrons are highly dynamic and commonly exhibit significant variations during geomagnetic storms (e.g., Reeves et al., 2003; Baker et al.,

2013; Thorne et al., 2013; Gu XD et al., 2020a; Murphy et al., 2020). Radiation electron losses are one of the most important physical processes of radiation belt electron dynamics and have been studied for decades (Shprits et al., 2006; Turner et al., 2014; Xiang Z et al., 2016; Zou ZY et al., 2020). The depletion of radiation belt electrons can be attributed to magnetopause shadowing, outward radial diffusion, and wave–particle interactions (e.g., Thorne et al., 2010; Matsumura et al., 2011; Ni BB et al., 2013; Hudson et al., 2014; Tu WC et al., 2014; Xiang Z et al., 2017b; Gu XD et al., 2020b; Liu ZY et al., 2020). However, the relative contributions of these physical mechanisms are not yet fully understood.

The electron losses caused by magnetopause shadowing occur when the magnetopause moves inward because of enhance-

ments in the solar wind dynamic pressure and because electrons at high *L*-shells find themselves at open drift shells (e.g., Turner et al., 2012a; Morley et al., 2013; Turner and Ukhorskiy, 2020). Electrons at lower *L*-shells move outward because of the sharp radial gradients of electron phase space density (PSD), and they experience decay (e.g., Keika et al., 2005; Shprits et al., 2006; Matsumura et al., 2011; Turner et al., 2012b; Glauert et al., 2014; Ukhorskiy et al., 2015; Tu WC et al., 2019). The electrons can also be scattered by various magnetospheric waves, including plasmaspheric hiss waves, chorus waves, magnetosonic waves, and electromagnetic ion cyclotron (EMIC) waves (e.g., Summers et al., 2007a, b; Thorne et al., 2010; Turner et al., 2014; Xiang Z et al., 2017a; Ni BB et al., 2019; Fu S et al., 2020). The EMIC waves are thought to play a particularly important role in radiation belt dropouts, during which the electron flux can decrease by several orders of magnitude within a few hours (e.g., Bortnik et al., 2006; Morley et al., 2010; Turner et al., 2012b; Cao X et al., 2017). A number of previous studies have reported that EMIC waves contribute significantly to multi-MeV electron (i.e., less than ~2 MeV) dropouts during geomagnetic storm main phases (e.g., Shprits et al., 2013, 2016, 2017; Kersten et al., 2014; Usanova et al., 2014; Ma Q et al., 2016; Su ZP et al., 2017; Xiang Z et al., 2017b, 2018). Electromagnetic ion cyclotron waves can lead to a strong loss of MeV electrons with timescales of <1 hour, whereas loss timescales of MeV electrons attributable to chorus and hiss waves are about a few days.

In this study, we investigated a radiation belt dropout event on 12–13 September 2014 by using high-resolution particle and wave measurements from Van Allen Probes. Three periods of this event (before the storm, the initial phase of the storm, and the main phase of the storm) were comprehensively studied to obtain the observational features during different phases of the geomagnetic storm. To distinguish the dominant loss mechanism in different spatial regions during different phases of the storm, the pitch angle distribution (PAD) of electron fluxes, the observations of EMIC waves, and the electron PSD drops at different μ and K (first and second adiabatic invariants) were analyzed. We provide the flux observations from satellites in Section 2 and analyze the calculated results of electron PSDs in Section 3. Section 4 presents a discussion of our results, and Section 5 summarizes the conclusions.

2. Event Overview

2.1 Solar Wind and Geomagnetic Conditions

This study focuses on a moderate geomagnetic storm with a minimum disturbance storm time (*Dst*) index around −100 nanoteslas (nT) that occurred after a solar wind dynamic pressure pulse event (increase of ~15 nanopascals (nPa) within 4 hours) on 12–13 September 2014. Figure 1 shows the corresponding solar wind dynamic pressure (P_{dyn}), interplanetary magnetic field (IMF B_z), auroral electrojet (*AE*) and *Dst* indices, and magnetopause standoff distance (from top to bottom). The solar wind parameters and geomagnetic indices were obtained from NASA's OMNIWeb (http://omniweb.gsfc.nasa.gov/) with a 1-min time resolution. The
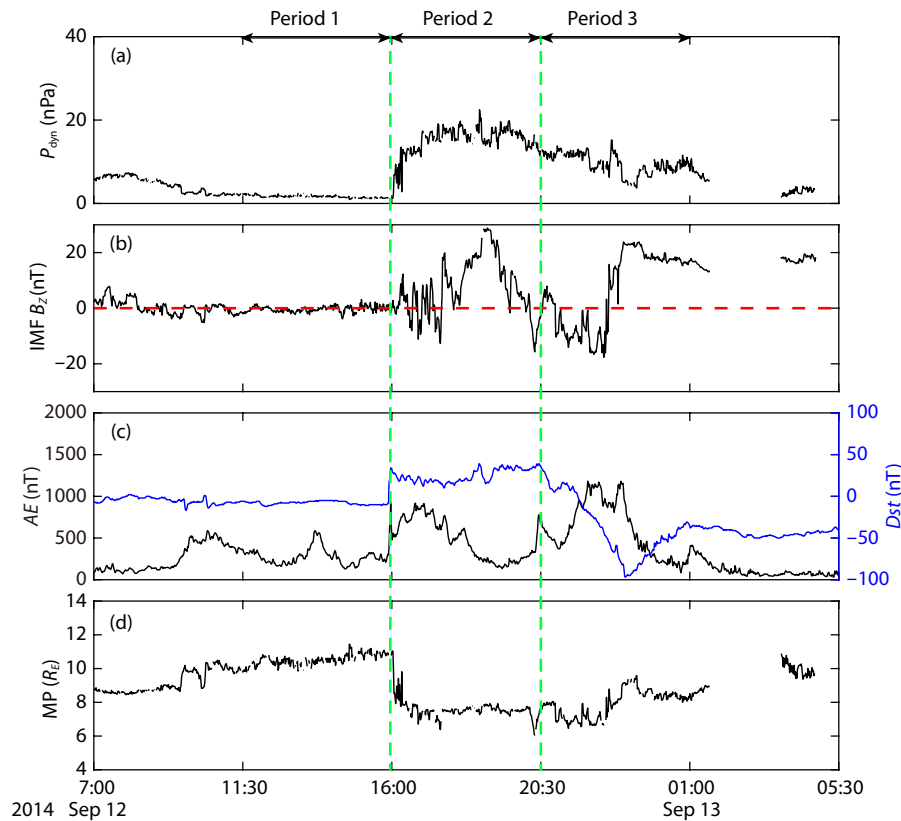

Figure 1.   Time series of solar wind parameters and geomagnetic indices from the OMNI database from 12 to 13 September 2014. From top to bottom: (a) solar wind dynamic pressure (P_{dyn}), (b) interplanetary magnetic field (IMF B_z), (c) auroral electrojet (*AE*, black line) and disturbance storm time (*Dst*) indices (blue line), and (d) magnetopause (MP) standoff distance (R_E).

initial phase of the storm began at ~16:00 universal time (UT) on 12 September 2014, as indicated by the sudden commencement of the storm, and the main phase occurred between ~20:30 and 23:00 UT. The *AE* index during this storm fluctuated considerably, with the maximum value reaching ~1,200 nT, indicating strong substorm activities. The magnitude of P_{dyn} increased, accompanied by an enhancement of the northward IMF B_z, and then it gradually decreased when the IMF B_z turned southward at ~20:00 UT on 12 September 2014. Figure 1d shows the standoff location of the magnetopause, which was calculated following the model of Shue et al. (1998). The figure shows that the magnetopause moved rapidly from ~11 earth radii (R_E) to ~7R_E along with the solar wind dynamic pulse and recovered to ~9R_E after the pulse interval.

We divided this event into three different periods, as indicated by the arrows at the top of Figure 1. Period 1 covers the time interval before the storm (i.e., before 16:00 UT on 12 September 2014), featured by P_{dyn} < 3 nPa, IMF B_z of ~0 nT, *Dst* of ~0 nT, and a magnetopause location of >10R_E. Period 2 corresponds to the initial phase of the storm (16:00–20:30 UT on 12 September 2014), which exhibited a strong P_{dyn} pulse, a mainly northward IMF B_z, sudden storm commencement and strong substorm activity, and inward intrusion of the magnetopause to ~7R_E. Period 3 started at the beginning of the main phase of the storm from 20:30 UT on 12 September 2014 to 01:00 UT on 13 September 2014, as characterized by a gradual decrease in P_{dyn}, a southward IMF B_z that subsequently turned northward, the approach of a *Dst* minimum and strong substorm activity, and recovery of the magnetopause to ~9R_E. Clearly, both the solar wind parameters and the geomagnetic activity were highly dynamic during the event under investigation, which could trigger distinct responses among radiation belt electrons in different spatial regions during different time intervals.

2.2 Electron Flux Observations
The NASA Van Allen Probes, launched on 30 August 2012, have a geosynchronous transfer orbit with an orbital period of ~9 hours, an inclination of 10.2°, a perigee of 1.09R_E, and an apogee of 5.77R_E. In this study, the pitch angle-resolved electron flux data obtained by a magnetic electron ion spectrometer (MagEIS; Blake et al., 2013) and a relativistic electron–proton telescope (REPT; Baker et al., 2013) were used to examine radiation belt electron distributions. Measurements based on the Electric and Magnetic Field Instruments Suite and Integrated Science (EMFISIS) instrument (Kletzing et al., 2013) were used to investigate magnetospheric plasma waves in detail.

Figure 2 shows electron fluxes with a 90° local pitch angle at energies of 4.2 MeV, 3.4 MeV, 2.1 MeV, 1,073 keV, 749 keV, 470 keV, 176 keV, and 54 keV (from top to bottom) observed by Van Allen Probes from 12 to 13 September 2014. We adopted background-corrected MagEIS data (Claudepierre et al., 2015) for <1.5 MeV electrons and REPT data for higher energy electrons.

A decrease in electron fluxes could be observed in multiple energy channels during both periods 2 and 3. However, the behavior differed between MeV electrons and hundreds of keV electrons. During period 2 (initial phase of the storm), the electron fluxes mainly decayed at *L* > 5 at almost all energy channels. During period 3 (main phase of the storm), the fluxes decayed more deeply at *L* > 4 and expanded to 3 < *L* < 4 for 2.1–4.2 MeV electrons. In contrast, lower energy electrons (e.g., 54 keV) exhibited a sharp enhancement at *L* < 4 instead of a flux decay.

The evolution of electron PADs measured by both Van Allen Probes from 12 to 13 September 2014 at *L* = 4, 4.5, and 5 (from left to right), with the three time bins (shaded areas) corresponding to periods 1 to 3, respectively, is displayed in Figure 3. At *L* = 4, electron fluxes at all energies mostly manifested 90°-peaked PADs instead of butterfly PADs. At *L* = 4.5, weak butterfly PADs for MeV electrons were observed during period 2, whereas no butterfly PADs occurred at lower energies. At *L* = 5, butterfly PADs occurred at almost all energy electrons during periods 2 and 3, which became more significant during period 2 when the magnetopause was compressed closer to the earth. This result suggests that the butterfly PADs were likely caused by magnetopause shadowing (e.g., Ni BB et al., 2020). In addition, the prompt enhancements of the electron fluxes at lower energies (e.g., 54 keV) at *L* < 4 were likely due to the substorm-induced electron injections.

To clearly exhibit the characteristics of electron flux PADs, we introduced a butterfly PAD index β (Ni BB et al., 2016a) as

$$\beta = \frac{j(90°)}{j_{avg}(j(<90°)_{max} : j(>90°)_{max})}, \qquad (1)$$

where *j* (90°) is the electron flux at a 90° pitch angle, *j* (<90°)$_{max}$ is the maximum electron flux at a <90° pitch angle, and *j* (>90°)$_{max}$ is the maximum electron flux at a >90° pitch angle. In this study, we set the threshold value of butterfly PADs as β = 0.95. A higher value of β indicates more 90°-peaked distributions.

Figure 4 shows the butterfly PAD index β as a function of electron energy and *L*-shells in periods 2 and 3. During period 2, the butterfly PADs were observed for a wide energy range at *L* > 4.5 and became sharper as *L* increased, whereas a slight change of PADs occurred at lower energies. The β value was larger during period 3 (Figure 4b) than during period 2 for almost all energy channels at *L* > 4.5. Unlike period 2, the >1MeV electron PADs tended to peak at a 90° pitch angle inside *L* = ~4.5 during period 3 (main phase of the storm, with IMF B_z turning from northward to southward). These observations indicate that the electron loss during period 3 could be caused by EMIC waves because EMIC waves scatter only high-energy electrons, producing 90°-peaked PADs (Ni BB et al., 2015a; Xiang Z et al., 2017a, 2019). Butterfly PADs were observed for almost all energies at *L* > 4.5 during both period 2 and period 3, indicating that magnetopause shadowing was potentially the main loss mechanism.

Figure 5 shows the evolution of electron flux radial profiles for different electron energies and pitch angles from 12 to 13 September 2014 by using REPT data (>2 MeV) and MagEIS data (<2 MeV) from Van Allen Probe B during color-coded orbit periods. Period 1
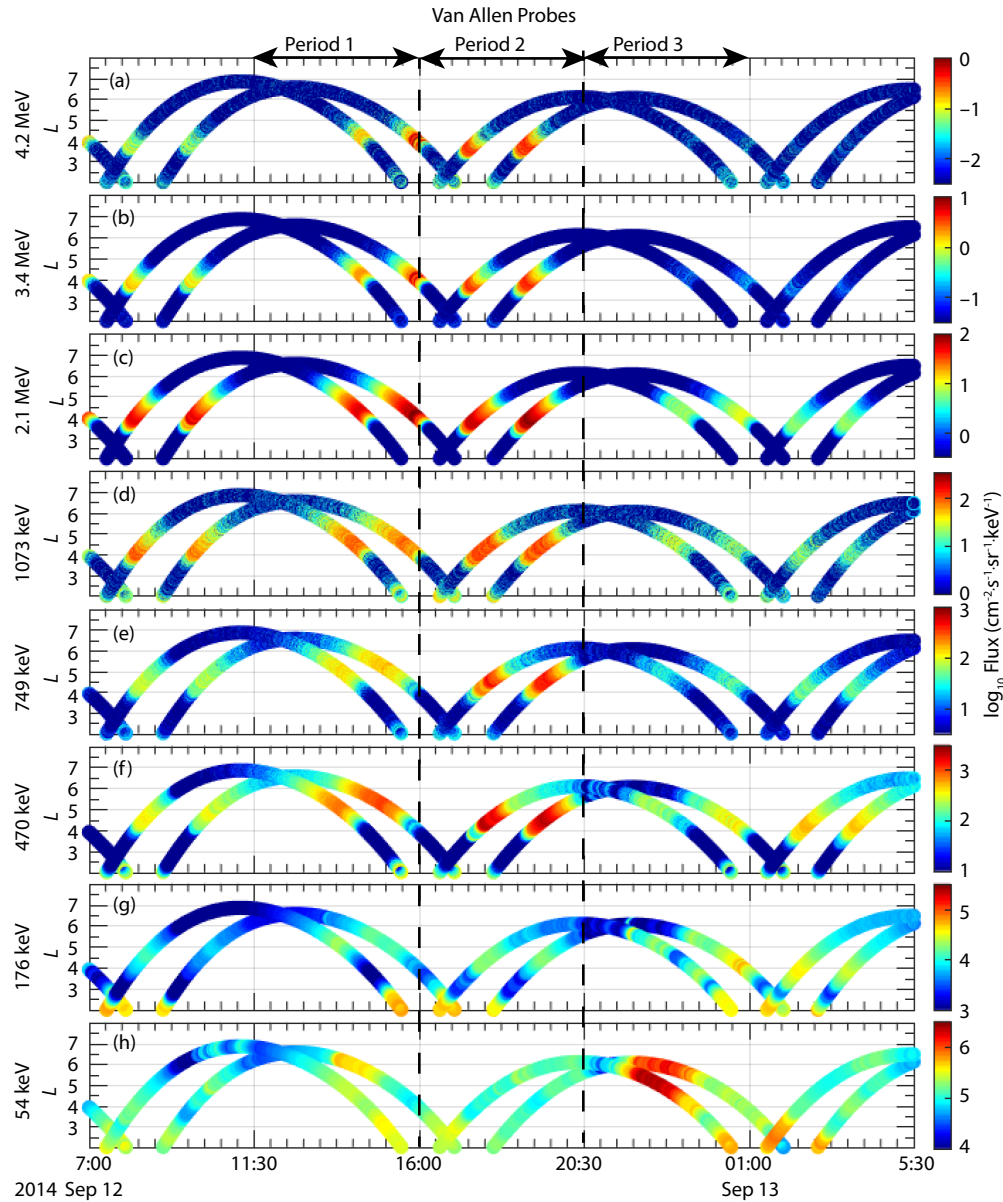
Figure 2. Fluxes of radiation belt electrons at a 90° local pitch angle for the indicated energies from 12 to 13 September 2014 based on observations from REPT (a–c) and MagEIS (d–h) onboard both Van Allen Probes. The range of period 1, period 2, and period 3 are the same as in Figure 1.

(green line) represents the initial conditions before the geomagnetic storm, whereas the purple and blue lines correspond to the aforementioned period 2 (initial phase of the storm) and period 3 (main phase of the storm), respectively. For electrons with a pitch angle larger than 50° (first three rows), the corresponding fluxes during period 2 were smaller than those for period 1 for >1 MeV electrons at $L > 4$. However, the fluxes were larger at a pitch angle less than 60° during period 2. For hundreds of keV electrons (right three columns), flux decreases were also observed at large pitch angles at $L > 5$. The ~90° pitch angle electron losses at a high L-shell were found for all electron energies during period 2. This was accompanied by a compressed magnetopause toward the Earth from ~11R_E to ~7R_E, as suggested by the rapidly increasing P_{dyn}, indicating that the electron losses were caused by magnetopause shadowing.

To clearly illustrate the electron losses from period 1 to period 3, the flux drops in relation to the L-shell are shown in Figure 6. The flux drops were obtained by subtracting the flux during period 2 from that during period 1 (purple line) and the flux during period 3 from that during period 2 (blue line) at given energies and pitch angles. The format of Figure 6 is the same as that of Figure 5. The decay of electron fluxes during period 2 compared with period 1 has been described previously. We focused on the flux drop from period 2 to period 3 shown in Figure 6, during which the storm entered the main phase and the orientation of IMF B_z changed from northward to southward. As shown in Figure 6, the electron flux drops were strongly dependent on the electron energy. For >1 MeV electrons (left three columns), the drops decreased with a decreasing electron pitch angle at $L > 5$, whereas the drops increased as the electron pitch angle decreased at $L < 5$. For all pitch
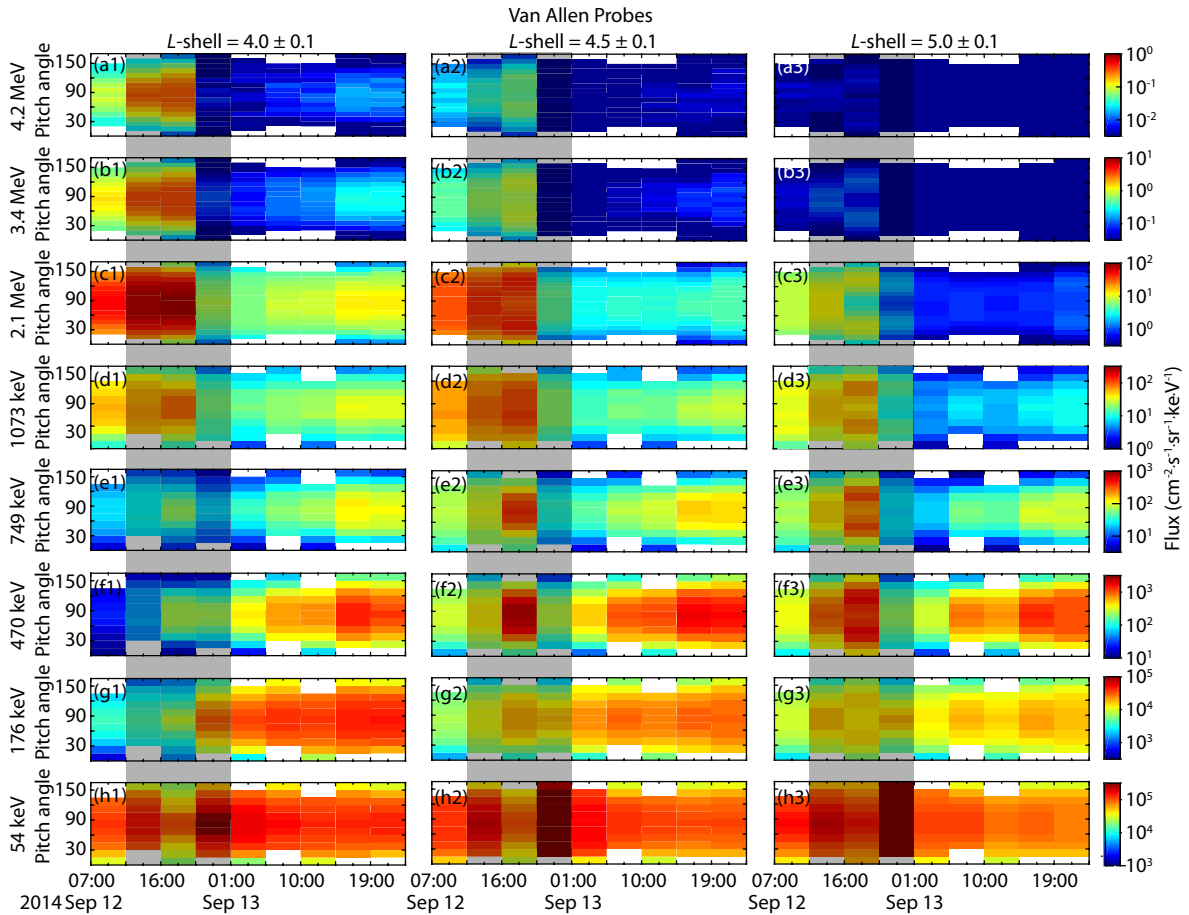
Ma X and Xiang Z et al.: Loss mechanisms of radiation belt dropout

Figure 3. The evolution of electron pitch angle distributions measured by REPT and MagEIS onboard both Van Allen Probes for the indicated energies at a given *L*-shell, with the three time bins (shaded areas) corresponding to periods 1 to 3, respectively.
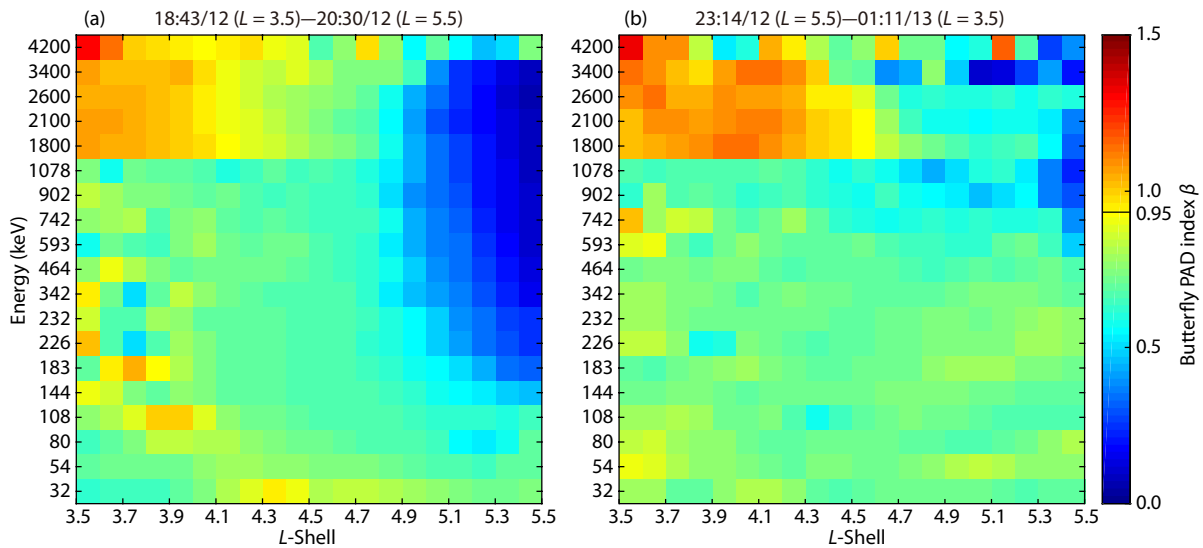

Figure 4. Butterfly PAD index β versus *L*-shell and energy during (a) period 2 and (b) period 3.

angles, a positive correlation was observed between the drops and electron energy. This strong dependence of electron flux drops on electron energy is consistent with electron loss attributable to scattering effects driven by EMIC waves, which can lead to top-hat PADs. Furthermore, EMIC waves were observed during period 2, as shown in Figure 7, supporting the conclusion that EM-IC wave scattering could have been the main loss mechanism during period 3. For hundreds of keV electrons (right three columns), the drops at *L* < 4 were less significant than those at higher *L*-shells and had no obvious pitch angle dependence.

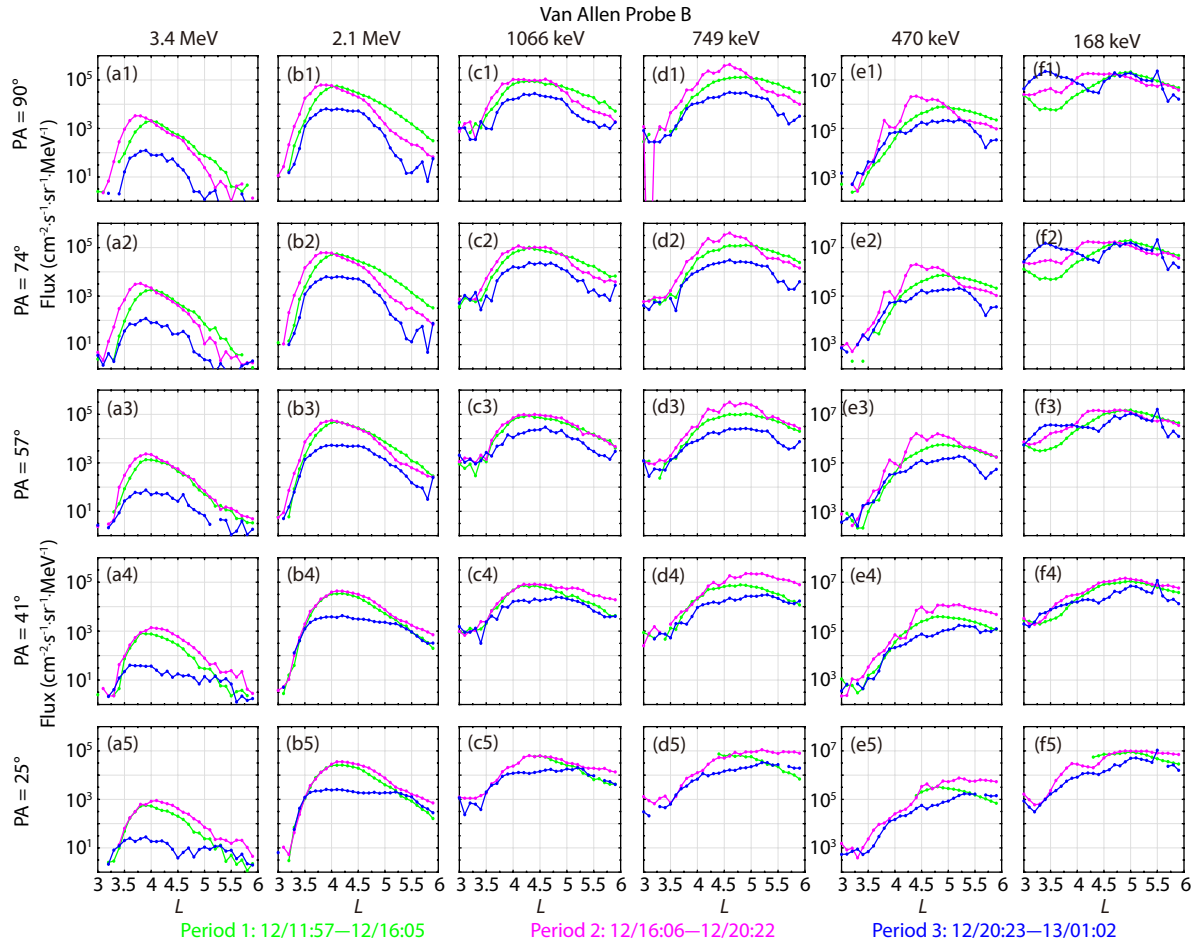**Ma X and Xiang Z et al.: Loss mechanisms of radiation belt dropout**

Figure 5. Radial profiles of the electron fluxes as a function of the L-shell at different electron energies, from left to right, (a1–a5) 3.4 MeV, (b1–b5) 2.1 MeV, (c1–c5) 1,066 keV, (d1–d5) 749 keV, (e1–e5) 470 keV, and (f1–f5) 168 keV, and pitch angles (PA), from top to bottom, (a1–f1) 90°, (a2–f2) 74°, (a3–f3) 57°, (a4–f4) 41°, and (a5–f5) 25°, from 11:57 UT on 12 September to 01:02 UT on 13 September 2014. The period of each electron flux radial profile is color coded and shown at the bottom of the figure.

3. Electron PSD Observations

To investigate the physical mechanism responsible for the flux dropouts of radiation belt electrons and to exclude the adiabatic effect associated with the change in magnetic field strength in space (Su ZP et al., 2015; Xiang Z et al., 2017b, 2018), the PSD of electrons in the outer radiation belt was examined in detail from 11:57 UT on 12 September 2014 to 01:02 UT on 13 September 2014. Figure 8 shows the evolution of electron PSD radial profiles at specified μ and K during this event. The values of μ increased from left to right, and the values of K increased from top to bottom. During period 2 (purple lines), which indicates the initial phase of the storm, the electron PSD decayed only weakly compared with period 1 at a lower K (e.g., $K = 0.02\ G^{1/2}R_E$ and 0.04 $G^{1/2}R_E$) and a higher L^* (e.g., $L^* > 5$). However, when the storm entered the main phase (period 3, blue lines), significant dropouts occurred for almost all μ and for higher K (e.g., $K > 0.08$ $G^{1/2}R_E$) at $L^* = 3.5$–5.3.

Figure 9 shows the PSD drops between different periods. The value of PSD drops illustrates the decay process of electron PSD, which was obtained by calculating the logarithm of the ratio of the previous period PSD to the later period PSD at the same L^*.

The red curves indicate the minimum electron resonant energies attributable to cyclotron resonance with H^+-band EMIC waves. The method and assumptions of Silin et al. (2011) were used to calculate the curves. Additionally, the dipole geomagnetic field model and the plasmaspheric density model (Sheeley et al., 2001) were adopted in the calculation. The representative parameters for H^+-band EMIC waves, with an upper cutoff wave frequency of 0.8 f_{cp} (where f_{cp} is the proton gyrofrequency) and an ion composition ratio $H^+ : He^+ : O^+$ of 0.85 : 0.1 : 0.05, were used following previous studies (e.g., Summers and Thorne, 2003; Summers et al., 2007b; Meredith et al., 2014; Ni BB et al., 2015b). The minimum resonant electron energies for H^+-band EMIC waves were the lowest among all three bands, indicating electrons that could be scattered efficiently by He^+- and O^+-band EMIC waves and by H^+-band EMIC waves (Young et al., 1981; Zhang XJ et al., 2016; Xiang Z et al., 2018).

Figure 9a–9d displays the evolution of PSD drops between period 1 and period 2. Figure 9a shows the evolution of PSD drops versus L^* at $K = 0.02\ G^{1/2}R_E$ and $\mu = 100$–3,600 MeV/G; the μ from 100 to 3,600 MeV/G are color coded. Phase space density drops occur only at $L^* > 5$ at $K = 0.02\ G^{1/2}R_E$. The PSD drops versus μ and K at $L^* = 3.9, 4.6,$ and 5.1 are shown in Figure 9b–9d, respectively. The val-
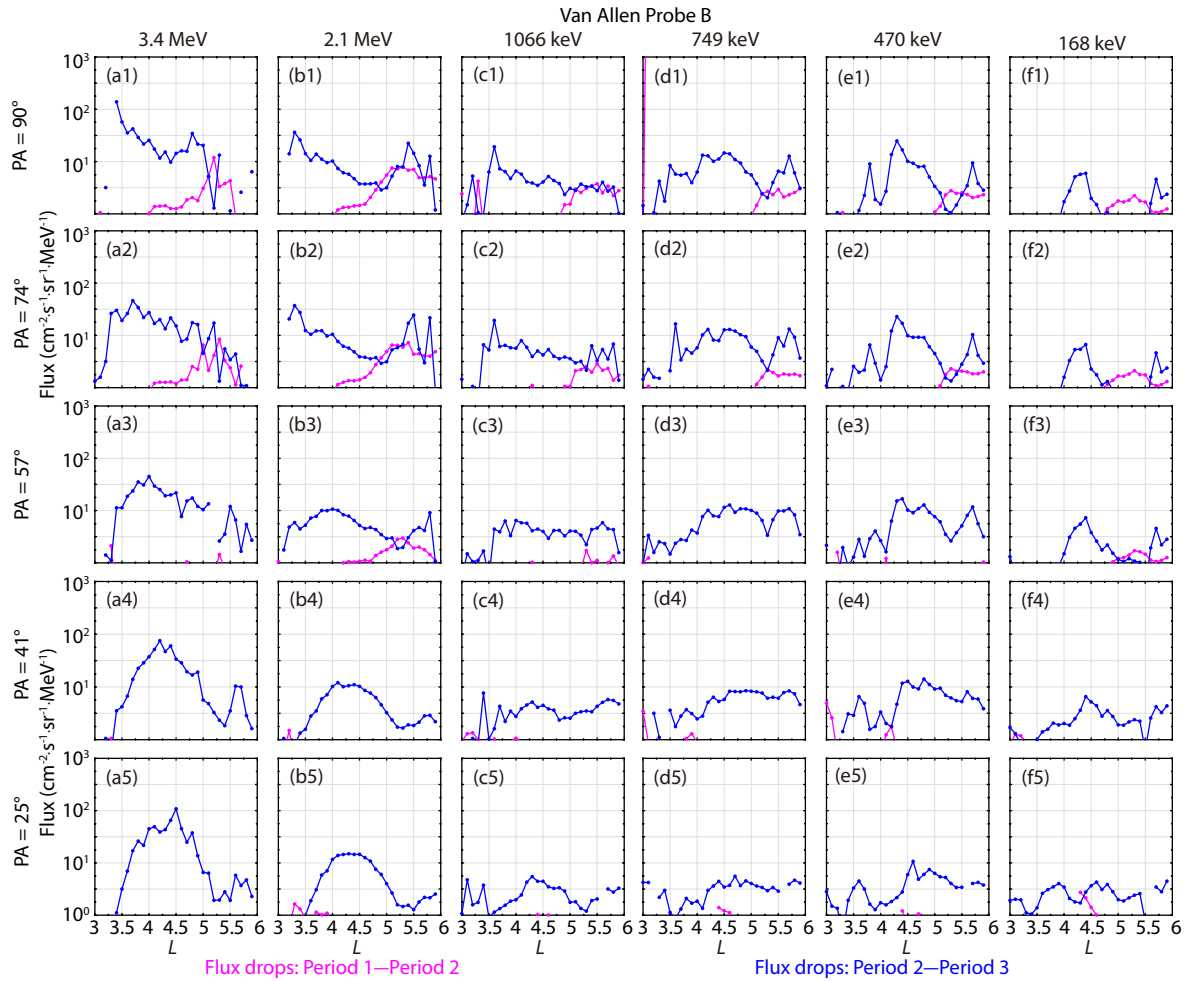
Van Allen Probe B

Figure 6. Electron flux drops as a function of the *L*-shell at different electron energies and pitch angles (PA) from 11:57 UT on 12 September to 01:02 UT on 13 September 2014. The energy and pitch angle in each panel are the same as in Figure 5.
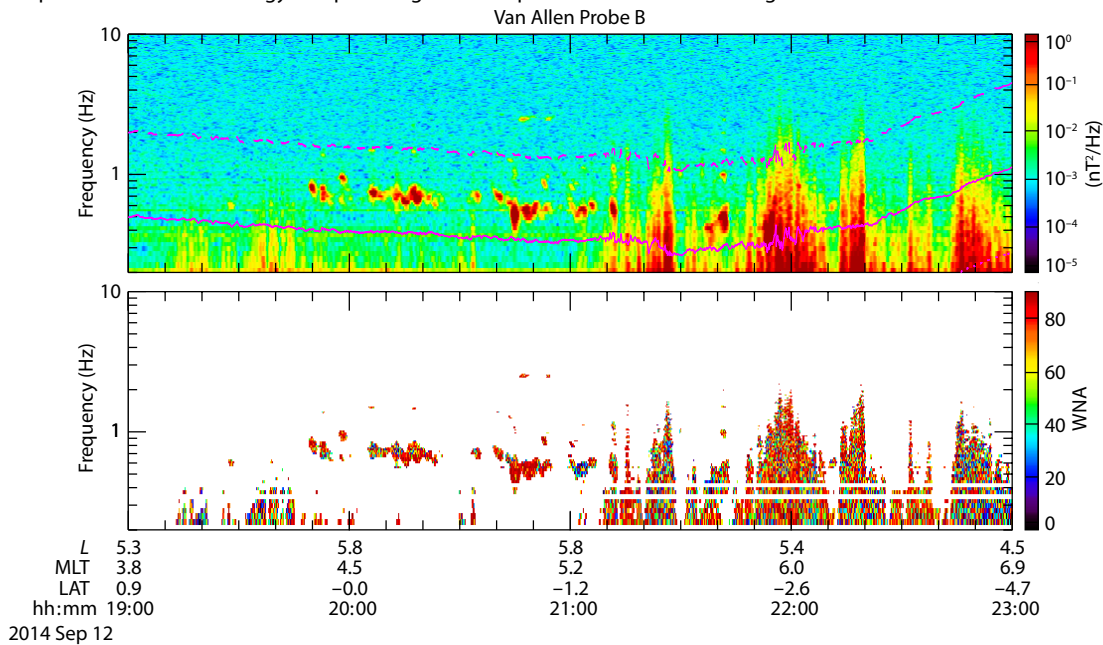

Figure 7. Electromagnetic ion cyclotron wave observations from 19:00 to 23:00 UT on 12 September 2014 by Van Allen Probe B. (a) The magnetic field power spectral density (H+ gyrofrequency: purple dashed line; He+ gyrofrequency: purple solid line) and (b) the wave normal angle (WNA).
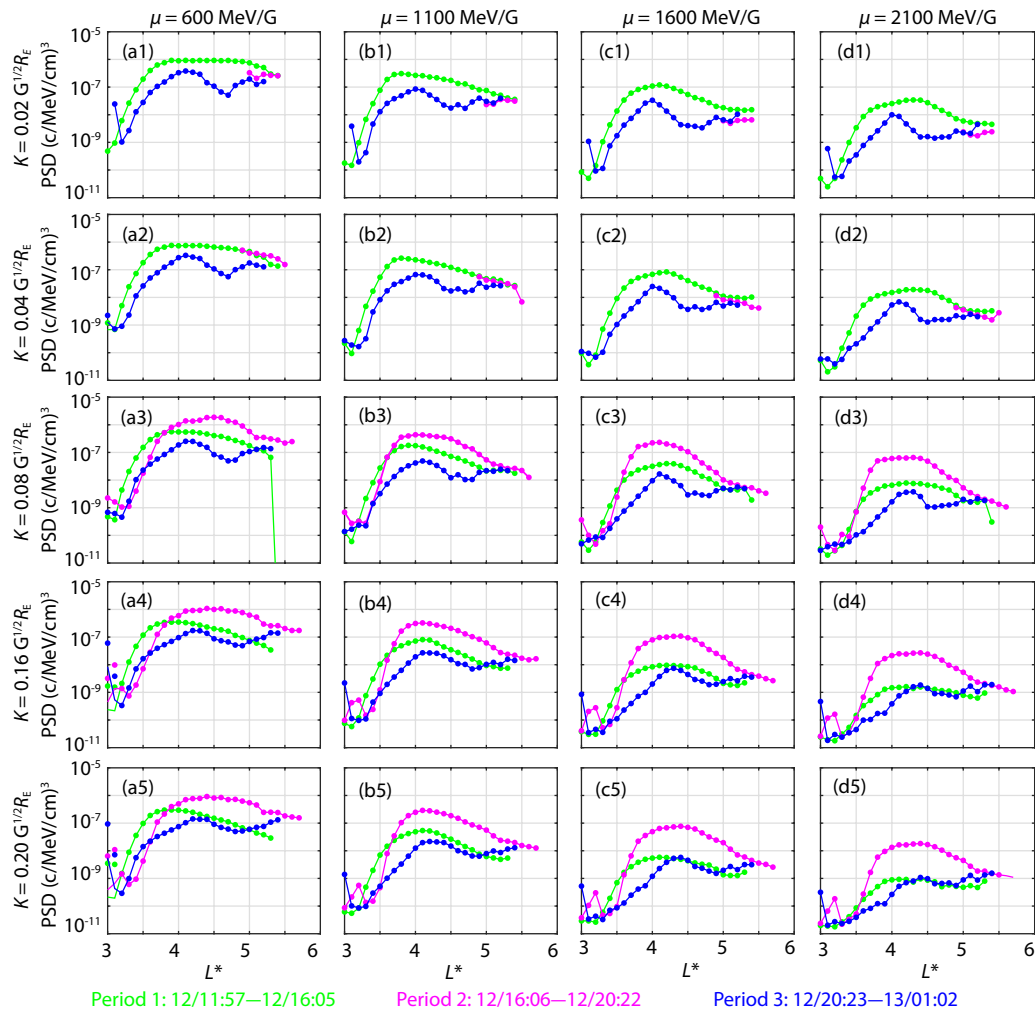
Ma X and Xiang Z et al.: Loss mechanisms of radiation belt dropout

Figure 8. Electron phase space density (PSD) radial profile for the different pairs of μ and K during the period from 11:57 UT on 12 September to 01:02 UT on 13 September 2014. The start and end times of each electron PSD radial profile are color coded.

ues of PSD drops almost equal zero at $L^* = 3.9$ and 4.6, whereas comparatively small PSD drops cover a wide range of μ for $K = 0.02$ and 0.04 $G^{1/2}R_E$ at $L^* = 5.1$ (Figure 9d), which is consistent with the results in Figure 9a. The decay shows no dependence on μ and a low value of K, confirming the loss characteristics as caused by magnetopause shadowing. However, the evolution of PSD drops between period 2 and period 3 is quite different from that between period 1 and period 2, as displayed in Figure 9e–9h. Figure 9e shows the evolution of PSD drops versus L^* at $\mu = 1,100$ MeV/G and $K = 0.02$–0.26 $G^{1/2}R_E$. Two drop peaks occur around $L^* = 3.9$ and $L^* = 4.6$, which are indicated by two dashed lines, respectively. These drop peaks also exist at other μ values, which indicates different mechanisms at different μ. Hence, we show the dependence of PSD drops with μ and K at $L^* = 3.9$, 4.6, and 5.1 in Figure 9f–9h. At $L^* = 3.9$, significant PSD drops occur above the red curves, which indicates that the EMIC wave scattering is stronger here. In Figure 9g, the results show significant PSD drops both above and below the red curves, and they form a distinct boundary along the red curve at $L^* = 4.6$. This result suggests that EMIC wave scattering is the main loss mechanism above the red curve, whereas some other loss mechanisms may be effective below the red curve around $L^* = 4.6$. At $L^* = 5.1$, the magnetopause

is still in a compressed state during the main phase of the storm (Figure 1d); therefore, magnetopause shadowing is effectively causing electron loss.

4. Discussion

The storm investigated in this study has been reported in previous studies. However, most of these studies have focused on long-lasting (>10-day) depletion after a rapid loss process. Jaynes et al. (2015) used GOES and Van Allen Probe data to examine the causes of the long-lasting depletion and suggested that the absence of chorus wave activity might explain the lack of any significant recovery following the initial rapid depletion. Ozeke et al. (2017) used an ultra low frequency wave radial diffusion model to simulate the variation in ultra-relativistic electron fluxes, and the excellent agreement between the observations and simulations highlighted the potentially dominant role of ultra low frequency transport. However, the mechanisms for rapid dropouts during the main phase of the storm remain unexplained.

In this study, we found that electron losses occurred in both the initial phase and the main phase of the storm, and each phase had a different orientation of IMF B_z. The characteristics of electron
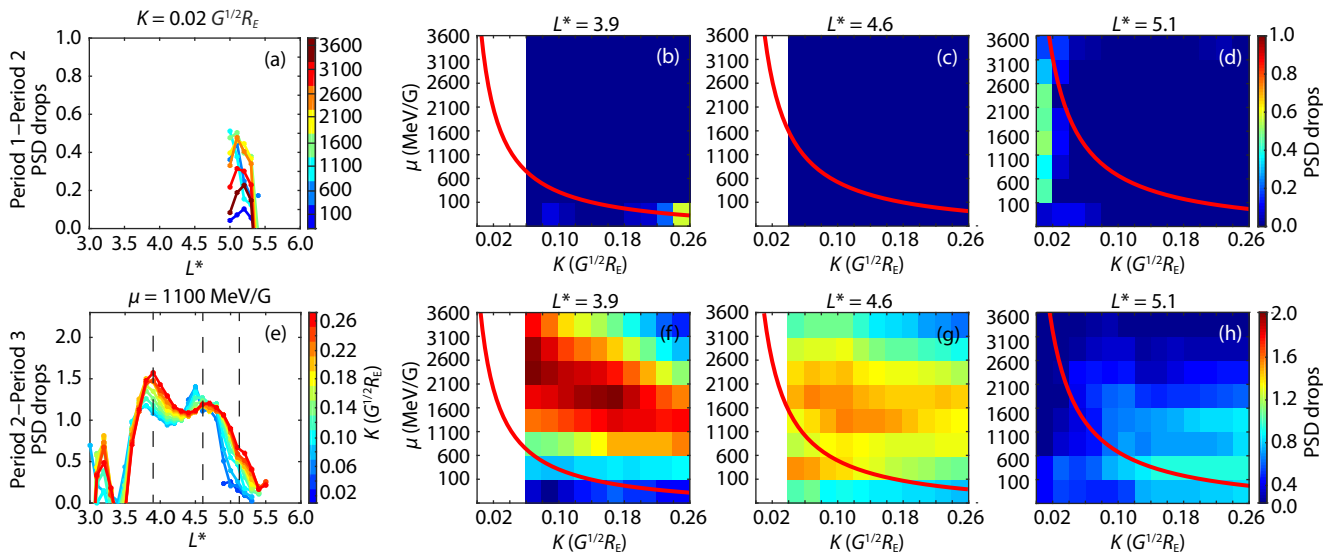
Ma X and Xiang Z et al.: Loss mechanisms of radiation belt dropout

Figure 9. Electron phase space density (PSD) drops observed between (a–d) periods 1 and 2 and between (e–h) periods 2 and 3. The red curves in panels b–d and f–h indicate the minimum electron resonant energies attributable to cyclotron resonance with H$^+$-band electromagnetic ion cyclotron (EMIC) waves, which have been mapped to the μ and K coordinates.

Table 1. Summary of the electron decay processes during the geomagnetic storm.

	Initial phase	Main phase
Solar wind & geomagnetic conditions	P_{dyn} increased rapidly to 23 nPa IMF B_z remained northward The AE index reached ~1,000 nT	P_{dyn} continued to decrease IMF B_z changed from northward to southward The AE index reached ~1,200 nT
Magnetopause	Dropped from ~11R_E to ~7R_E	~6R_E
Radiation belt electron fluxes	PA >60°: significant losses occurred for > 1 MeV electrons at L > 4 and for hundreds of keV electrons at L > 5 PA <60°: no loss occurred for almost all energy at L > 4.5	Electron fluxes decreased dramatically at L > 4 across a wide energy range; losses at lower L-shells were observed only for >1 MeV electrons Fluxes lost more as the PA decreased and the energy range increased for >1 MeV electrons
Pitch angle distributions	Butterfly PADs occurred at L > 4.5	PAD characteristics tended toward 90°-peaked PADs for >1 MeV electrons at L < 4 Butterfly distributions were weaker for lower energies at L > 4.7
Radiation belt electron PSD	Weak PSD drops occurred only in low K around L^* = 5.1	Two PSD drop peaks occurred around L^* = 3.9 and L^* = 4.6 PSD drops were above the red curve around L^* = 3.9 PSD drops occurred both above and below the red curve around L^* = 4.6 Small PSD drops occurred at L^* = 5.1
Possible mechanisms	Magnetopause shadowing was dominant at L > 5	Magnetopause shadowing occurred at L > 5 A combination of EMIC wave scattering and outward radial diffusion occurred around L = 4.6 PA scattering by EMIC waves occurred at L < 4

Notes: P_{dyn}, solar wind dynamic pressure; IMF B_z, interplanetary magnetic field; AE index, auroral electrojet index; R_E, Earth radii; PA, pitch angle; PAD, pitch angle distribution; PSD, phase space density; EMIC waves, electromagnetic ion cyclotron waves.

loss processes during the two periods were different, which indicates there are different mechanisms for the entire radiation belt electron loss process. To clearly understand the underlying physics responsible for the loss processes during the initial phase and main phase of the storm, we have summarized some information from the two periods in Table 1, including parameters of the solar wind and geomagnetic conditions, magnetopause standoff locations, evolution of the radiation belt electron flux and PSD, and the corresponding possible dominant electron loss mechanisms.

During the initial phase of this storm, the magnetopause was compressed by the rapid increase in the P_{dyn}. Significant electron loss was observed over a wide range of energies outside L = ~5, and more electron losses were observed near the equator, causing butterfly PADs. Phase space density drops occurred only in low K around L^* = 5.1, as shown in Figure 9d, fitting the electron flux loss characteristic during the initial phase of the storm. These phenomena are consistent with electron losses caused by magnetopause shadowing. During the main phase of the storm, the

evolution of electron fluxes and PSD drops both differed from the previous period. At $L > 5$, magnetopause shadowing caused by the compressed magnetopause continued from the initial phase to the main phase. The electron PADs presented a typical butterfly distribution in a wide energy range. Around $L = 4.6$, the energy dependence of the electron flux evolution began to emerge. For >1 MeV electrons, the flux drops increased as the pitch angle decreased, resulting in 90°-peaked PADs. The PSD drops are divided into two parts by the red curve in Figure 9. This indicates minimum resonant electron energies of H^+-band EMIC waves, suggesting that EMIC wave scattering loss was the main dropout mechanism above the red curve. For drops below the red curve, direct loss by magnetopause shadowing was insignificant because the last closed drift shell rarely reached such low L^* regions (Xiang Z et al., 2018). Persistent magnetopause shadowing from the initial phase to the main phase at a higher L-shell then produced flux gradients and resulted in outward radial diffusion, which could cause electrons loss from the lower L-shell. At $L < 4$, significant dropouts occurred mainly for >1 MeV electrons, leading to 90°-peaked PADs. Phase space density drops all occurred above the red curve. During the main phase of the storm, the orientation of the IMF B_z turned from northward to southward. And with a southward IMF, the magnetic reconnection could occur at the subsolar magnetopause (Roelof and Sibeck, 1993; Shue et al., 1998; Suvorova et al., 1999, 2005; Ma X et al., 2017), which could enhance the anisotropic ($T_\perp > T_{//}$) distribution of energetic ions, and then contribute to exciting the EMIC waves. Electromagnetic ion cyclotron waves were also observed by Van Allen Probe B during the main phase. All the above evidence demonstrates that EMIC wave scattering was stronger at the $L < 4$ region.

Our observational results are consistent with the findings of Ni BB et al. (2016b), who investigated the flux variations during 40 solar wind dynamic pressure pulse events between September 2012 and December 2014 based on the radiation belt electron flux measurements from five satellites. These findings suggest that large depletions in radiation belt electron fluxes are more likely to occur in association with the P_{dyn} pulse under southward IMF B_z conditions. Therefore, magnetopause shadowing and outward radial diffusion are more likely to dominate at higher L-shells, whereas pitch angle scattering by EMIC waves may be the main loss mechanism at lower L-shells during the main phase of a storm.

5. Conclusions

In this study, high-quality measurements from Van Allen Probes were used to investigate the loss mechanisms of a radiation belt electron dropout event during a moderate geomagnetic storm. Electron flux losses occurred during both the initial and main phases of the storm under different orientations of the interplanetary magnetic field.

The main conclusions can be summarized as follows:

(1) During the initial phase of the storm, the electron flux decay was independent of electron energy at $L > 4.5$, accompanied by butterfly PADs. This result suggests that magnetopause shadowing may be the dominant loss mechanism at $L > 4.5$ during the initial phase of the storm.

(2) During the main phase of the storm, electron fluxes decreased dramatically at $L > 4$ over a wide energy range because of the effect of magnetopause shadowing, whereas at lower L-shells, dropouts were observed only for >1 MeV electrons. Moreover, the electrons exhibited 90°-peaked PADs for >1 MeV electrons at $L < 4$. These features and EMIC wave observations support the view that EMIC wave-induced electron scattering plays an important role in dropouts during the main phase of a storm at $L < 4$.

(3) By evaluating the (μ, K) dependence of electron PSD drops and calculating the minimum electron resonant energies of H^+-band EMIC waves, we found that almost all the PSD drops around $L^* = 3.9$ occurred above the minimum electron resonant energies of H^+-band EMIC waves. This may be due mainly to the scattering of EMIC waves, whereas the drops around $L^* = 4.6$ could be observed both above and below the minimum electron resonant energies of H^+-band EMIC waves, which could have resulted from a combination of EMIC wave scattering and outward radial diffusion.

In this study, the electron loss event was investigated primarily from an observational perspective. Recently, various diffusion or convection–diffusion models have been developed to simulate the wave–particle interactions and magnetopause shadowing loss in the outer radiation belt (e.g., Fok et al., 2008; Tu WC et al., 2014; Drozdov et al., 2015; Kang et al., 2016; Xiang Z et al., 2020). Therefore, to deepen our physical understanding of the electron loss mechanisms underlying the radiation belt dropout event during the 12 September 2014 storm, it would be valuable to perform numerical simulations based on these models to reproduce the electron flux variations for detailed data-model comparisons, which is left for future study.

References

Baker, D. N., Kanekal, S. G., Hoxie, V. C., Batiste, S., Bolton, M., Li, X., Elkington, S. R., Monk, S., Reukauf, R., … Cervelli, B. (2013). The Relativistic Electron-Proton Telescope (REPT) instrument on board the Radiation Belt Storm Probes (RBSP) spacecraft: Characterization of Earth's radiation belt high-energy particle populations. *Space Sci. Rev., 179*(1-4), 337–381. https://doi.org/10.1007/s11214-012-9950-9

Blake, J. B., Carranza, P. A., Claudepierre, S. G., Clemmons, J. H., Crain, Jr. W. R., Dotan, Y., Fennell, J. F., Fuentes, F. H., Galvan, R. M., … Zakrzewski, M. P. (2013). The Magnetic Electron Ion Spectrometer (MagEIS) instruments aboard the Radiation Belt Storm Probes (RBSP) spacecraft. *Space Sci. Rev.*, *179*(1-4), 383–421. https://doi.org/10.1007/s11214-013-9991-8

Bortnik, J., Thorne, R. M., O'Brien, T. P., Green, J. C., Strangeway, R. J., Shprits, Y. Y., and Baker, D. N. (2006). Observation of two distinct, rapid loss mechanisms during the 20 November 2003 radiation belt dropout event. *J. Geophys. Res. Space Phys.*, *111*(A12), A12216. https://doi.org/10.1029/2006JA011802

Cao, X., Shprits, Y. Y., Ni, B. B., and Zhelavskaya, I. S. (2017). Scattering of ultra-relativistic electrons in the Van Allen radiation belts accounting for hot plasma effects. *Sci. Rep.*, *7*, 17719. https://doi.org/10.1038/s41598-017-17739-7

Claudepierre, S. G., O'Brien, T. P., Blake, J. B., Fennell, J. F., Roeder, J. L., Clemmons, J. H., Looper, M. D., Mazur, J. E., Mulligan, T. M., … Larsen, B. A. (2015). A background correction algorithm for Van Allen Probes MagEIS electron flux measurements. *J. Geophys. Res. Space Phys.*, *120*(7), 5703–5727. https://doi.org/10.1002/2015JA021171

Drozdov, A. Y., Shprits, Y. Y., Orlova, K. G., Kellerman, A. C., Subbotin, D. A., Baker, D. N., Spence, H. E., and Reeves, G. D. (2015). Energetic, relativistic, and ultrarelativistic electrons: Comparison of long-term VERB code simulations with Van Allen Probes measurements. *J. Geophys. Res. Space Phys.*, *120*(5), 3574–3587. https://doi.org/10.1002/2014JA020637

Fok, M. C., Horne, R. B., Meredith, N. P., and Glauert, S. A. (2008). Radiation Belt Environment model: Application to space weather nowcasting. *J. Geophys. Res. Space Phys.*, *113*(A3), A03S08. https://doi.org/10.1029/2007JA012558

Fu, S., Yi, J., Ni, B. B., Zhou, R. X., Hu, Z. J., Cao, X., Gu, X. D., and Guo, D. Y. (2020). Combined scattering of radiation belt electrons by low-frequency hiss: Cyclotron, Landau, and bounce resonances. *Geophys. Res. Lett.*, *47*(5), e2020GL086963. https://doi.org/10.1029/2020GL086963

Glauert, S. A., Horne, R. B., and Meredith, N. P. (2014). Simulating the Earth's radiation belts: Internal acceleration and continuous losses to the magnetopause. *J. Geophys. Res. Space Phys.*, *119*(9), 7444–7463. https://doi.org/10.1002/2014JA020092

Gu, X. D., Xia, S. J., Fu, S., Xiang, Z., Ni, B. B., Guo, J. G., and Cao, X. (2020a). Dynamic responses of radiation belt electron fluxes to magnetic storms and their correlations with magnetospheric plasma wave activities. *Astrophy. J.*, *891*(2), 127. https://doi.org/10.3847/1538-4357/ab71fc

Gu, X. D., He, Y., Ni, B. B., Fu, S., Hua, M., and Xiang, Z. (2020b). Scattering of radiation belt electrons caused by wave-particle interactions with magnetosonic waves associated with plasma density drop. *Chinese J. Geophys.* (in Chinese), *63*(6), 2121–2130. https://doi.org/10.6038/cjg2020N0384

Hudson, M. K., Baker, D. N., Goldstein, J., Kress, B. T., Paral, J., Toffoletto, F. R., and Wiltberger, M. (2014). Simulated magnetopause losses and Van Allen Probe flux dropouts. *Geophys. Res. Lett.*, *41*(4), 1113–1118. https://doi.org/10.1002/2014GL059222

Jaynes, A. N., Baker, D. N., Singer, H. J., Rodriguez, J. V., Loto'aniu, T. M., Ali, A. F., Elkington, S. R., Li, X., Kanekal, S. G., … Reeves, G. D. (2015). Source and seed populations for relativistic electrons: Their roles in radiation belt changes. *J. Geophys. Res. Space Phys.*, *120*(9), 7240–7254. https://doi.org/10.1002/2015JA021234

Kang, S. B., Fok, M. C., Glocer, A., Min, K. W., Choi, C. R., Choi, E., and Hwang, J. (2016). Simulation of a rapid dropout event for highly relativistic electrons with the RBE model. *J. Geophys. Res. Space Phys.*, *121*(5), 4092–4102. https://doi.org/10.1002/2015JA021966

Keika, K., Nosé, M., Ohtani, S. I., Takahashi, K., Christon, S. P., and McEntire, R. W. (2005). Outflow of energetic ions from the magnetosphere and its contribution to the decay of the storm time ring current. *J. Geophys. Res. Space Phys.*, *110*(A9), A09210. https://doi.org/10.1029/2004JA010970

Kersten, T., Horne, R. B., Glauert, S. A., Meredith, N. P., Fraser, B. J., and Grew, R. S. (2014). Electron losses from the radiation belts caused by EMIC waves. *J. Geophys. Res. Space Phys.*, *119*(11), 8820–8837. https://doi.org/10.1002/2014JA020366

Kletzing, C. A., Kurth, W. S., Acuna, M., MacDowall, R. J., Torbert, R. B., Averkamp, T., Bodet, D., Bounds, S. R., Chutter, M., … Tyler, J. (2013). The electric and magnetic field instrument suite and integrated science (EMFISIS) on RBSP. *Space Sci. Rev.*, *179*(1-4), 127–181. https://doi.org/10.1007/s11214-013-9993-6

Liu, Z. Y., Ni, B. B., Fu, S., Xiang, Z., Guo, J. G., Cao, X., Gu, X. D., Yi, J., Guo, Y. J., … Wang, J. Z. (2020). Multi-satellite observations of storm-time radiation belt electron phase space density variations. *Chinese J. Geophys.* (in Chinese), *63*(6), 2149–2158. https://doi.org/10.6038/cjg2020N0414

Ma, Q., Li, W., Thorne, R. M., Nishimura, Y., Zhang, X. J., Reeves, G. D., Kletzing, C. A., Kurth, W. S., Hospodarsky, G. B., … Angelopoulos, V. (2016). Simulation of energy-dependent electron diffusion processes in the Earth's outer radiation belt. *J. Geophys. Res. Space Phys.*, *121*(5), 4217–4231. https://doi.org/10.1002/2016JA022507

Ma, X., Lu, J. Y., and Wang, M. (2017). Pressure balance across the magnetopause during the solar wind event on 5 June 1998. *Planet. Space Sci.*, *139*, 11–17. https://doi.org/10.1016/j.pss.2017.02.014

Matsumura, C., Miyoshi, Y., Seki, K., Saito, S., Angelopoulos, V., and Koller, J. (2011). Outer radiation belt boundary location relative to the magnetopause: Implications for magnetopause shadowing. *J. Geophys. Res. Space Phys.*, *116*(A6), A06212. https://doi.org/10.1029/2011JA016575

Meredith, N. P., Horne, R. B., Kersten, T., Fraser, B. J., and Grew, R. S. (2014). Global morphology and spectral properties of EMIC waves derived from CRRES observations. *J. Geophys. Res. Space Phys.*, *119*(7), 5328–5342. https://doi.org/10.1002/2014JA020064

Morley, S. K., Friedel, R. H. W., Cayton, T. E., and Noveroske, E. (2010). A rapid, global and prolonged electron radiation belt dropout observed with the Global Positioning System constellation. *Geophys. Res. Lett.*, *37*(6), L06102. https://doi.org/10.1029/2010GL042772

Morley, S. K., Henderson, M. G., Reeves, G. D., Friedel, R. H. W., and Baker, D. N. (2013). Phase space density matching of relativistic electrons using the Van Allen probes: REPT results. *Geophys. Res. Lett.*, *40*(18), 4798–4802. https://doi.org/10.1002/grl.50909

Murphy, K. R., Mann, I. R., Sibeck, D. G., Rae, I. J., Watt, C. E. J., Ozeke, L. G., Kanekal, S. G., and Baker, D. N. (2020). A framework for understanding and quantifying the loss and acceleration of relativistic electrons in the outer radiation belt during geomagnetic storms. *Space Wea.*, *18*(5), e2020SW002477. https://doi.org/10.1029/2020SW002477

Ni, B. B., Bortnik, J., Thorne, R. M., Ma, Q. L., and Chen, L. J. (2013). Resonant scattering and resultant pitch angle evolution of relativistic electrons by plasmaspheric hiss. *J. Geophys. Res. Space Phys.*, *118*(12), 7740–7751. https://doi.org/10.1002/2013JA019260

Ni, B. B., Zou, Z. Y., Gu, X. D., Zhou, C., Thorne, R. M., Bortnik, J., Shi, R., Zhao, Z. Y., Baker, D. N., … Li, X. L. (2015a). Variability of the pitch angle distribution of radiation belt ultrarelativistic electrons during and following intense geomagnetic storms: Van Allen Probes observations. *J. Geophys. Res. Space Phys.*, *120*(6), 4863–4876. https://doi.org/10.1002/2015JA021065

Ni, B. B., Cao, X., Zou, Z. Y., Zhou, C., Gu, X. D., Bortnik, J., Zhang, J. C., Fu, S., Zhao, Z. Y., … Xie, L. (2015b). Resonant scattering of outer zone relativistic electrons by multiband EMIC waves and resultant electron loss time scales. *J. Geophys. Res. Space Phys.*, *120*(9), 7357–7373. https://doi.org/10.1002/2015JA021466

Ni, B. B., Zou, Z. Y., Li, X. L., Bortnik, J., Xie, L., and Gu, X. D. (2016a). Occurrence characteristics of outer zone relativistic electron butterfly distribution: A survey of Van Allen Probes REPT measurements. *Geophys. Res. Lett.*, *43*(11), 5644–5652. https://doi.org/10.1002/2016GL069350

Ni, B. B., Xiang, Z., Gu, X. D., Shprits, Y. Y., Zhou, C., Zhao, Z. Y., Zhang, X. G., and Zuo, P. B. (2016b). Dynamic responses of the Earth's radiation belts during periods of solar wind dynamic pressure pulse based on normalized superposed epoch analysis. *J. Geophys. Res. Space Phys.*, *121*(9), 8523–8536. https://doi.org/10.1002/2016JA023067

Ni, B. B., Huang, H., Zhang, W. X., Gu, X. D., Zhao, H., Li, X. L., Baker, D., Fu, S., Xiang, Z., and Cao, X. (2019). Parametric sensitivity of the formation of reversed electron energy spectrum caused by Plasmaspheric Hiss. *Geophys. Res. Lett.*, *46*(8), 4134–4143. https://doi.org/10.1029/2019GL082032

Ni, B. B., Yan, L., Fu, S., Gu, X. D., Cao, X., Xiang, Z., and Zhang, Y. N. (2020). Distinct formation and evolution characteristics of outer radiation belt electron butterfly pitch angle distributions observed by Van Allen Probes. *Geophys. Res. Lett.*, *47*(4), e2019GL086487. https://doi.org/10.1029/2019GL086487

Ozeke, L. G., Mann, I. R., Murphy, K. R., Sibeck, D. G., and Baker, D. N. (2017). Ultra-relativistic radiation belt extinction and ULF wave radial diffusion: Modeling the September 2014 extended dropout event. *Geophys. Res. Lett.*, *44*(6), 2624–2633. https://doi.org/10.1002/2017GL072811

Reeves, G. D., McAdams, K. L., Friedel, R. H. W., and O'Brien, T. P. (2003). Acceleration and loss of relativistic electrons during geomagnetic storms. *Geophys. Res. Lett.*, *30*(10), 1529. https://doi.org/10.1029/2002GL016513

Roelof, E. C., and Sibeck, D. G. (1993). Magnetopause shape as a bivariate function of interplanetary magnetic field B_z and solar wind dynamic pressure. *J. Geophys. Res. Space Phys.*, *98*(A12), 21421–21450. https://doi.org/10.1029/93JA02362

Sheeley, B. W., Moldwin, M. B., Rassoul, H. K., and Anderson, R. R. (2001). An empirical plasmasphere and trough density model: CRRES observations. *J. Geophys. Res. Space Phys.*, *106*(A11), 25631–25641. https://doi.org/10.1029/2000JA000286

Shprits, Y. Y., Thorne, R. M., Friedel, R., Reeves, G. D., Fennell, J., Baker, D. N., and Kanekal, S. G. (2006). Outward radial diffusion driven by losses at magnetopause. *J. Geophys. Res. Space Phys.*, *111*(A11), A11214. https://doi.org/10.1029/2006JA011657

Shprits, Y. Y., Subbotin, D., Drozdov, A., Usanova, M. E., Kellerman, A., Orlova, K., Baker, D. N., Turner, D. L., and Kim, K. C. (2013). Unusual stable trapping of the ultrarelativistic electrons in the Van Allen radiation belts. *Nat. Phys.*, *9*(11), 699–703. https://doi.org/10.1038/nphys2760

Shprits, Y. Y., Drozdov, A. Y., Spasojevic, M., Kellerman, A. C., Usanova, M. E., Engebretson, M. J., Agapitov, O. V., Zhelavskaya, I. S., Raita, T. J., … Aseev, N. A. (2016). Wave-induced loss of ultra-relativistic electrons in the Van Allen radiation belts. *Nat. Commun.*, *7*, 12883. https://doi.org/10.1038/ncomms12883

Shprits, Y. Y., Kellerman, A., Aseev, N., Drozdov, A. Y., and Michaelis, I. (2017). Multi-MeV electron loss in the heart of the radiation belts. *Geophys. Res. Lett.*, *44*(3), 1204–1209. https://doi.org/10.1002/2016GL072258

Shue, J. H., Song, P., Russell, C. T., Steinberg, J. T., Chao, J. K., Zastenker, G., Vaisberg, O. L., Kokubun, S., Singer, H. J., … Kawano, H. (1998). Magnetopause location under extreme solar wind conditions. *J. Geophys. Res. Space Phys.*, *103*(A8), 17691–17700. https://doi.org/10.1029/98JA01103

Silin, I., Mann, I. R., Sydora, R. D., Summers, D., and Mace, R. L. (2011). Warm plasma effects on electromagnetic ion cyclotron wave MeV electron interactions in the magnetosphere. *J. Geophys. Res. Space Phys.*, *116*(A5), A05215. https://doi.org/10.1029/2010JA016398

Su, Z. P., Zhu, H., Xiao, F. L., Zong, Q. G., Zhou, X. Z., Zheng, H. N., Wang, Y. M., Wang, S., Hao, Y. X., … Wygant, J. R. (2015). Ultra-low-frequency wave-driven diffusion of radiation belt relativistic electrons. *Nat. Commun.*, *6*, 10096. https://doi.org/10.1038/ncomms10096

Su, Z. P., Gao, Z. L., Zheng, H. N., Wang, Y. M., Wang, S., Spence, H. E., Reeves, G. D., Baker, D. N., and Wygant, J. R. (2017). Rapid loss of radiation belt relativistic electrons by EMIC waves. *J. Geophys. Res. Space Phys.*, *122*(10), 9880–9897. https://doi.org/10.1002/2017JA024169

Summers, D., and Thorne, R. M. (2003). Relativistic electron pitch-angle scattering by electromagnetic ion cyclotron waves during geomagnetic storms. *J. Geophys. Res. Space Phys.*, *108*(A4), 1143. https://doi.org/10.1029/2002JA009489

Summers, D., Ni, B. B., and Meredith, N. P. (2007a). Timescales for radiation belt electron acceleration and loss due to resonant wave-particle interactions: 1. Theory. *J. Geophys. Res. Space Phys.*, *112*(A4), A04206. https://doi.org/10.1029/2006JA011801

Summers, D., Ni, B. B., and Meredith, N. P. (2007b). Timescales for radiation belt electron acceleration and loss due to resonant wave-particle interactions: 2. Evaluation for VLF chorus, ELF hiss, and electromagnetic ion cyclotron waves. *J. Geophys. Res. Space Phys.*, *112*(A4), A04207. https://doi.org/10.1029/2006JA011993

Suvorova, A., Dmitriev, A., Chao, J. K., Thomsen, M., and Yang, Y. H. (2005). Necessary conditions for geosynchronous magnetopause crossings. *J. Geophys. Res. Space Phys.*, *110*(A1), A01206. https://doi.org/10.1029/2003JA010079

Suvorova, A. V., Dmitriev, A. V., and Kuznetsov, S. N. (1999). Dayside magnetopause models. *Radiat. Meas.*, *30*(5), 687–692. https://doi.org/10.1016/S1350-4487(99)00220-6

Thorne, R. M., Ni, B. B., Tao, X., Horne, R. B., and Meredith, N. P. (2010). Scattering by chorus waves as the dominant cause of diffuse auroral precipitation. *Nature*, *467*(7318), 943–946. https://doi.org/10.1038/nature09467

Thorne, R. M., Li, W., Ni, B., Ma, Q., Bortnik, J., Baker, D. N., Spence, H. E., Reeves, G. D., Henderson, M. G., … Angelopoulos, V. (2013). Evolution and slow decay of an unusual narrow ring of relativistic electrons near *L*~3 2 following the September 2012 magnetic storm. *Geophys. Res. Lett.*, *40*(14), 3507–3511. https://doi.org/10.1002/grl.50627

Tu, W. C., Cunningham, G. S., Chen, Y., Morley, S. K., Reeves, G. D., Blake, J. B., and Spence, H. (2014). Event-specific chorus wave and electron seed population models in DREAM3D using the Van Allen Probes. *Geophys. Res. Lett.*, *41*(5), 1359–1366. https://doi.org/10.1002/2013GL058819

Tu, W. C., Xiang, Z., and Morley, S. K. (2019). Modeling the magnetopause shadowing loss during the June 2015 dropout event. *Geophys. Res. Lett.*, *46*(16), 9388–9396. https://doi.org/10.1029/2019GL084419

Turner, D. L., Morley, S. K., Miyoshi, Y., Ni, B. B., and Huang, C. L. (2012a). Outer radiation belt flux dropouts: Current understanding and unresolved questions. In: D. Summers, et al. (Eds.), Dynamics of the Earth's Radiation Belts and Inner Magnetosphere (pp. 195-211). Washington: AGU. https://doi.org/10.1029/2012GM001310

Turner, D. L., Shprits, Y., Hartinger, M., and Angelopoulos, V. (2012b). Explaining sudden losses of outer radiation belt electrons during geomagnetic storms. *Nat. Phys.*, *8*(3), 208–212. https://doi.org/10.1038/nphys2185

Turner, D. L., Angelopoulos, V., Morley, S. K., Henderson, M. G, Reeves, G. D., Li, W., Baker, D. N., Huang, C. L., Boyd, A., … Rodriguez, J. V. (2014). On the cause and extent of outer radiation belt losses during the 30 September 2012 dropout event. *J. Geophys. Res. Space Phys.*, *119*(3), 1530–1540. https://doi.org/10.1002/2013JA019446

Turner, D. L., and Ukhorskiy, A. Y. (2020). Outer radiation belt losses by magnetopause incursions and outward radial transport: New insight and outstanding questions from the Van Allen Probes era. In: A. N. Jaynes, et al. (Eds.), The Dynamic Loss of Earth's Radiation Belts (pp. 1-28). Amsterdam: Elsevier. https: //doi.org/10.1016/B978-0-12-813371-2.00001-9

Ukhorskiy, A. Y., Sitnov, M. I., Millan, R. M., Kress, B. T., Fennell, J. F., Claudepierre, S. G., and Barnes, R. J. (2015). Global storm time depletion of the outer electron belt. *J. Geophys. Res. Space Phys.*, *120*(4), 2543–2556. https://doi.org/10.1002/2014JA020645

Usanova, M. E., Drozdov, A., Orloval, K., Mann, R., Shprits, Y., Robertson, M. T., Turner, D. L., Milling, D. K., Kale, A., … Wygant, J. (2014). Effect of EMIC waves on relativistic and ultrarelativistic electron populations: Ground-based and Van Allen Probes observations. *Geophys. Res. Lett.*, *41*(5), 1375–1381. https://doi.org/10.1002/2013GL059024

Xiang, Z., Ni, B. B., Zhou, C., Zou, Z. Y., Gu, X. D., Zhao, Z. Y., Zhang, X. G., Zhang, X. X., Zhang, S. Y., … Reeves, G. (2016). Multi-satellite simultaneous observations of magnetopause and atmospheric losses of radiation belt electrons during an intense solar wind dynamic pressure pulse. *Ann. Geophys.*, *34*(5), 493–509. https://doi.org/10.5194/angeo-34-493-2016

Xiang, Z., Tan, J. Q., Ni, B. B., Gu, X. D., Cao, X., Zou, Z. Y., Zhou, C., Fu, S.,... Wang, H. (2017a). A statistical analysis of the global distribution of plasmaspheric hiss based on Van Allen Probes wave observations. *Acta Phys. Sin.* (in Chinese), *66*(3), 039401. https://doi.org/10.7498/aps.66.039401

Xiang, Z., Tu, W. C., Li, X. L., Ni, B. B., Morley, S. K., and Baker, D. N. (2017b). Understanding the mechanisms of radiation belt dropouts observed by Van Allen Probes. *J. Geophys. Res. Space Phys.*, *122*(10), 9858–9879. https://doi.org/10.1002/2017JA024487

Xiang, Z., Tu, W. C., Ni, B. B., Henderson, M. G., and Cao, X. (2018). A statistical survey of radiation belt dropouts observed by Van Allen Probes. *Geophys. Res. Lett.*, *45*(16), 8035–8043. https://doi.org/10.1029/2018GL078907

Xiang, Z., Li, X. L., Selesnick, R., Temerin, M. A., Ni, B. B., Zhao, H., Zhang, K., and Khoo, L. Y. (2019). Modeling the quasi-trapped electron fluxes from Cosmic

Ray Albedo Neutron Decay (CRAND). *Geophys. Res. Lett.*, *46*(4), 1919–1928. https://doi.org/10.1029/2018GL081730

Xiang, Z., Li, X. L., Temerin, M. A., Ni, B. B., Zhao, H., Zhang, K., and Khoo, L. Y. (2020). On energetic electron dynamics during geomagnetic quiet times in Earth's inner radiation belt due to atmospheric collisional loss and CRAND as a source. *J. Geophys. Res. Space Phys.*, *125*(2), e2019JA027678. https://doi.org/10.1029/2019JA027678

Young, D. T., Perraut, S., Roux, A., De Villedary, C., Gendrin, R., Korth, A., Kremser, G., and Jones, D. (1981). Wave-particle interactions near Ω_{He+} observed on GEOS 1 and 2 1. Propagation of ion cyclotron waves in He$^+$-rich plasma. *J. Geophys. Res. Space Phys.*, *86*(A8), 6755–6772. https://doi.org/10.1029/JA086iA08p06755

Zhang, X. J., Li, W., Ma, Q., Thorne, R. M., Angelopoulos, V., Bortnik, J., Chen, L., Kletzing, C. A., Kurth, W. S., … Fennell, J. F. (2016). Direct evidence for emic wave scattering of relativistic electrons in space. *J. Geophys. Res. Space Phys.*, *121*(7), 6620–6631. https://doi.org/10.1002/2016JA022521

Zou, Z. Y., Zuo, P. B., Ni, B. B., Gao, Z. L., Wang, G., Zhao, Z. Y., Feng, X. S., and Wei, F. S. (2020). Two-step dropouts of radiation belt electron phase space density induced by a magnetic cloud event. *Astrophys. J. Lett.*, *895*(1), L24. https://doi.org/10.3847/2041-8213/ab9179